ARTICLE	**Open Access**

Creating robotic intelligence using multistimuli-responsive cobalt-doped manganese oxide

Runni Wu[1], Kin Wa Kwan [1], Chi Hin Mak [1] and Alfonso Hing Wan Ngan[1]

Abstract

Compact material constructs possessing some degree of built-in intelligence via the exhibition of complex functionalities in response to easily deliverable stimuli are highly desirable for material-powered robots. We report here a visible light-driven, dual-responsive material of cobalt-doped manganese dioxide ($Co\text{-}MnO_2$), which exhibits high actuation performance in terms of speed and power requirement and decreased electrical resistivity under light illumination. The actuation properties are fine-tunable by controlling the amount of Co doping, followed by an electrochemical treatment to activate the actuation, and the resistance change conveniently serves as a built-in feedback signal for controlling the actuation. Utilizing these properties, compact microrobotic devices capable of self-sensing visible light intensities of ~4 mW/cm^2 to perform complex motions along multiple selectable configurational pathways are fabricated. Intelligent robotic functions, including self-adapting load lifting, object sorting, and on-demand structural stiffening, are demonstrated in these devices. The concept demonstrated here opens up a perspective of creating robotic intelligence using multistimuli-responsive materials.

Introduction

Material-driven robots, including insect-scale, soft robots, are expected to perform complex tasks impossible for humans or to produce biomimicking functions hardly achievable by conventional "mechatronic" devices[1]. These robots are functionalized by integrating various smart materials that are stimuli-responsive, small and compliant, and to achieve motility or motion, smart actuating materials that operate under various stimuli have been extensively studied[2]. Among these, materials actuated by electrical[3] and visible light signals[4] offer better prospects because of the easy delivery and control in comparison with temperature or humidity changes. Light-actuated materials, in particular, allow wireless triggering[5–7] and flexible modulation of the local shape deformation within a single device body[8]. Other actuating materials can respond to multiple stimuli[9], be tailored to perform various motions[10], or exhibit multiple functions[11–13], but for building versatile microrobots, a more intelligent material system that can actuate and sense simultaneously to perform feedback-controlled, self-adapting motions along multiple selectable configurational pathways is highly desirable. In previous sensing-actuating systems, specific resistive[14–17], capacitive[18,19], or opto-mechanical/electronic[20–22] sensors were added externally in a circuitry to provide a feedback signal to regulate the actuator. However, this requires complicated integration of the sensor and the actuator, and some systems lack an easy read-out electrical feedback variable for achieving complex functionality. Recently, a few material solutions have been introduced to offer self-sensing and other capabilities; for example, a special templating synthesis technique was developed to enable multifunctional origami metallic backbones to be fabricated with built-in resistive heating, strain sensing, and antenna capabilities[23], and carbon-based actuators have been designed with a self-sensing function for humidity-, thermo-, or piezo-induced resistivity changes[24–26]. However, the responses of these devices can only be driven by temperature/humidity changes or strong infrared (IR) light of intensity >1 sun, and their

Correspondence: Kin Wa Kwan (kkwkwan@connect.hku.hk)
[1]Department of Mechanical Engineering, The University of Hong Kong, Pokfulam Road, Hong Kong, PR China

actuation is sometimes low (deflection of <180°)[24–26] or slow (>10 s)[26].

Therefore, to make practical microrobotic systems, it is necessary to develop high-performing and intelligent artificial muscles, namely, materials that exhibit not only fast and large actuation under low-power stimulus input but also a real-time sensing ability. Moreover, it would be advantageous if the actuation motion and structural stiffness could be tunable so that more modes of actions and tasks could be performed. In this paper, we introduce the concept of creating intelligence in robotic devices using a multistimuli-responsive material, namely, cobalt-doped manganese oxide (Co-MnO$_2$), that possesses the abovementioned desired qualities. Co-MnO$_2$, which is fabricated by simple electrodeposition and activated by a one-step electrochemical treatment, exhibits high actuation performance, with high magnitude (curvatures up to 1.7 mm^{-1}), fast speed (~100 ms for one loop), and good reversibility, in response to a broad band of light signals covering the visible to IR range in humidity-rich environments. Under light stimulation, Co-MnO$_2$ also exhibits a second response of reducing the electrical resistivity, which can be conveniently used as a built-in feedback signal to achieve self-sensing intelligence without externally added sensing elements. The actuation is also tunable by controlling the Co:Mn ratio in the material, which is utilized in this work to design robotic devices with multiple selectable configurational pathways. Moreover, the intelligence of muscle stiffness adjustment for performing load-demanding robotic functions is also realizable by a specific set of Co-MnO$_2$ patterns built in the artificial muscle construct to stiffen the muscle "on-demand", thus solving the compliance problem commonly found in other smart material systems. In the following, material characterization, actuation, and the sensing performance of Co-MnO$_2$ will first be presented, followed by a discussion of the intelligent microrobotic devices made from this material.

Experimental section
Fabrication of actuators and actuation tests

A Ni layer and a Au layer were first electrodeposited (see more details in Supporting Text S1 and Fig. S1 in the Supplementary information), and Co-MnO$_2$ was then electrodeposited on the Au side. The electrodeposition baths for Co-MnO$_2$ were mixtures of two solutions A (CoSO$_4$, CH$_3$COONa, and Na$_2$SO$_4$, all at 0.15 M) and B (C$_4$H$_6$MnO$_4$·4H$_2$O and Na$_2$SO$_4$, both at 0.15 M) at ratios of A:B = 1:5, 1:2, and 2:1. An anodic current density of 0.545 mA/cm^2 was applied for 15 min under mild stirring. All chemicals were of reagent grade and purchased from Sigma-Aldrich. The "activation treatment" was performed by immersing the freshly fabricated actuators into 1 M NaOH for cyclic voltammetry (CV) from −0.2 to 0.5 V at

a scan rate of 25 mV/s for five cycles. The "activated" actuator was then triggered at room temperature and a relative humidity (RH) of 95% by NIR or Vis light from a xenon arc lamp (Zolix, HPS-500XA). All electrodeposition and CV procedures were conducted by an electrochemical workstation (Corrtest, CS350).

Sensing characterization

The self-integrated sensing-actuating unit in "Self-integrated sensing and actuating construct" was made by attaching a Au-Ni electrode onto a Co-MnO$_2$ actuator prepared from an electrolyte with Co:Mn = 5:1. A constant current of 1 μA was applied to the sensor by an electrochemical workstation (Corrtest, CS350), which also recorded the corresponding voltage change under stimulation, and the average resistance change rate was calculated. For the devices in "Smart load-lifting system" and "Smart robotic finger with feedback-controlled multiple configurational pathways", the resistance of the sensor comprising two active Co-MnO$_2$/Au-Ni bilayers facing each other was constantly measured, with the feedback resistance change rate $\dot{R}$ calculated by an Arduino program. The light intensity was adjusted according to the difference between the calculated resistance decrease rate $|\dot{R}|$ and the set value $C_{|\dot{R}|}$ by simple proportional control, in which the current supplied to the LED was tuned by an Arduino digital pin combined with a transistor (2SD526).

Material characterization

Scanning electron microscopy (SEM) and transmission electron microscopy (TEM) were carried out on a Hitachi S-4800 microscope and a FEI Tecnai G20 Scanning TEM. Fourier transform infrared (FTIR) analysis was performed on a Bruker Tensor 27 spectrometer, and contact angle measurements of DI water on Co-MnO$_2$ surfaces were carried out on a 100SB Sindatek instrument. Atomic force microscopy (AFM) examination was carried out on a Bruker Multi-Mode 8 AFM. The surface temperature of the Co-MnO$_2$ actuator was measured by a FLIR SC7700M IR camera. In-plane grazing incidence X-ray diffraction was performed on a Rigaku SmartLab diffractometer with an incidence angle of 0.5° using a monochromatic Cu Kα source. Raman scattering spectroscopy using a Spectra Pro HRS-300 spectrometer and X-ray photoelectron spectrometry (XPS) on a Kratos Axis Ultra spectrometer using a monochromatic Al Kα source were also performed.

Results
Multistimuli, multiresponsive nature of Co-MnO$_2$ and the activation treatment

The actuator configuration comprises an active layer of Co-MnO$_2$ electrodeposited on top of a passive supporting
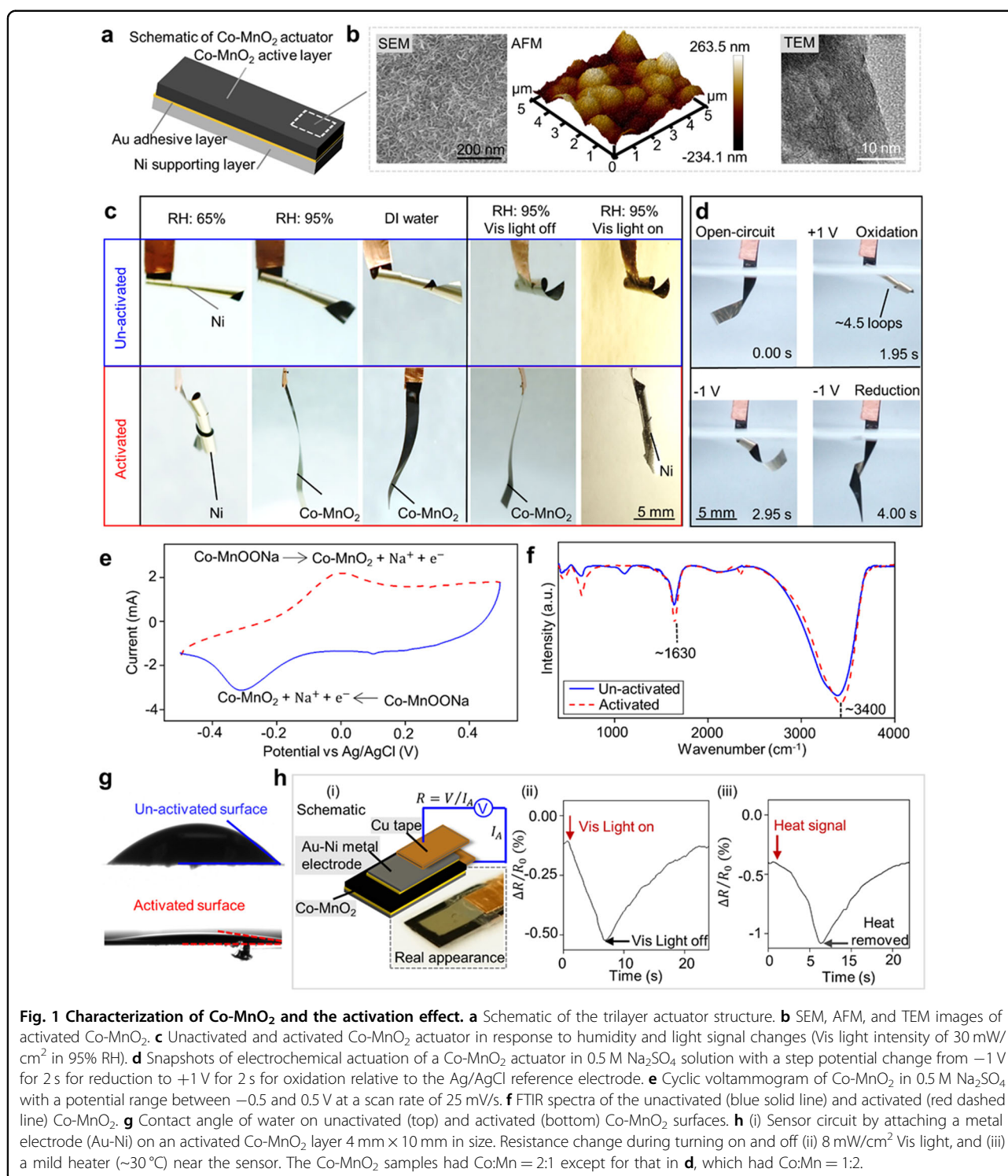
Fig. 1 Characterization of Co-MnO$_2$ and the activation effect. a Schematic of the trilayer actuator structure. **b** SEM, AFM, and TEM images of activated Co-MnO$_2$. **c** Unactivated and activated Co-MnO$_2$ actuator in response to humidity and light signal changes (Vis light intensity of 30 mW/cm^2 in 95% RH). **d** Snapshots of electrochemical actuation of a Co-MnO$_2$ actuator in 0.5 M Na$_2$SO$_4$ solution with a step potential change from −1 V for 2 s for reduction to +1 V for 2 s for oxidation relative to the Ag/AgCl reference electrode. **e** Cyclic voltammogram of Co-MnO$_2$ in 0.5 M Na$_2$SO$_4$ with a potential range between −0.5 and 0.5 V at a scan rate of 25 mV/s. **f** FTIR spectra of the unactivated (blue solid line) and activated (red dashed line) Co-MnO$_2$. **g** Contact angle of water on unactivated (top) and activated (bottom) Co-MnO$_2$ surfaces. **h** (i) Sensor circuit by attaching a metal electrode (Au-Ni) on an activated Co-MnO$_2$ layer 4 mm × 10 mm in size. Resistance change during turning on and off (ii) 8 mW/cm^2 Vis light, and (iii) a mild heater (~30 °C) near the sensor. The Co-MnO$_2$ samples had Co:Mn = 2:1 except for that in **d**, which had Co:Mn = 1:2.

layer of metallic Ni, with an intermediate Au layer to enhance adhesion (Fig. 1a). The energy dispersive X-ray line mapping reveals a relatively even distribution of Co and Mn throughout the structure, and the thicknesses of the Ni, Au, and active layers are ~1, 0.1, and 2 μm (Fig. S1). SEM combined with AFM (Fig. 1b) shows that

the electrodeposited Co-MnO$_2$ consists of densely packed needles[27] with a rough and solid surface morphology. TEM (Fig. 1b) reveals a crumpled, amorphous, and disordered microstructure. The freshly prepared actuator curls significantly toward the active layer (forward direction) at both low (65%) and high (95%) RH and when

immersed in water, which corresponds to a contractive state of the Co-MnO$_2$ active material (Fig. 1c). In this state, the actuator exhibits a weak response to light or humidity changes, as shown in Fig. 1c, and the same behavior is found for actuators made from pure MnO$_2$. To activate the actuation response to humidity and Vis light signals, the actuators were treated under CV in 1 M NaOH from −0.5 to 0.2 V at a scan rate of 25 mV/s. During such a treatment, the actuator gradually uncurls and opens toward the supporting Ni layer (backward direction) in an irreversible manner. After the activation, the actuator curls backward when put in an environment of high RH, e.g., ~95% and water, as shown in Fig. 1c, corresponding to a volume expansion of Co-MnO$_2$. Upon exposure to a lower RH of ~65% (Fig. 1c), the actuator quickly and autonomously curls forward, corresponding to contraction of Co-MnO$_2$. The humidity-responsive actuation gives an angular deflection of ~1260° for the 20-mm-long actuator, and similar actuation can also be induced by a visible (Vis) light signal, as shown in Fig. 1c. In addition, the material can also be electrochemically actuated in 0.5 M Na$_2$SO$_4$ electrolyte (Fig. 1d). From the CV, the current–potential characteristics (Fig. 1e) indicate that the actuation mechanism is due to Na$^+$ insertion and extraction, which cause a volume change of Co-MnO$_2$, similar to that in the recently discovered manganese dioxide (MnO$_2$) actuator[28]. Additionally, during the CV scan in Na$_2$SO$_4$, no obvious irreversible expansion is observed, as in the activation treatment under NaOH with the same potential window applied.

To study the activation mechanism of the light actuation, activated and unactivated samples of Co-MnO$_2$ were analyzed by FTIR spectroscopy and contact angle measurement. For the FTIR spectra, as shown in Fig. 1f, the larger intensity of the feature peak at 1630 cm^{-1} for the activated sample indicates an increase in adsorbed or intercalated water molecules, and the blueshift at 3200–3400 cm^{-1} indicates more free water molecules compared to the unactivated sample[29]. The measured contact angle for the unactivated sample is ~40°, while that of the activated sample is in the range of <5° (Fig. 1g), which indicates complete water wetting. Therefore, the activation treatment evidently makes the Co-MnO$_2$ surface highly hydrophilic, with a much higher affinity to water molecules than the unactivated state. This well agrees with the expansion behavior upon exposure to high RH and immersion in water (Fig. 1c), and this behavior can be explained by the adsorption/intercalation of water molecules in the activated state of Co-MnO$_2$. Additionally, from the relatively similar XRD and Raman spectra (Fig. S2) for both samples, it is found that no extra new phase appears after the activation, but the crystallinity of activated Co-MnO$_2$ decreases. The XPS results (Figs. S3–S5 and Tables S1–S3) indicate that the activation causes

Co(II) and Mn(II)/Mn(III) to oxidize into Co(III) and Mn(III)/Mn(IV) (Figs. S3 and S4 and Tables S1 and S2), and there is incorporation of Na$^+$ into the turbostratic structure of MnO$_6$ basal planes (Fig. S2). Therefore, the activation effect is likely caused by an increase in water molecules adsorbed or intercalated due to Na$^+$ incorporation[30]. Moreover, the presence of Co enhances the effect compared to the pure MnO$_2$ sample, probably due to an increase in water adsorbed or intercalated into the Na-birnessite, as proven by a thermogravimetric analysis that shows more weight loss for the Co-doped sample[31]. The Supplementary materials (Text S2 and Figs. S2–S7) provide a more detailed discussion regarding the activation effect of Co-MnO$_2$.

Under Vis light illumination, it is found that the electrical resistance (R) of Co-MnO$_2$ decreases, which can be utilized as a built-in feedback signal for a sensing capability. Figure 1h shows the reduction in R under Vis light illumination at an ultralow intensity of 8 mW/cm^2. The measurement of R was performed by a circuit comprising a Au-Ni electrode manually attached on top of the activated Co-MnO$_2$ layer, with a constant current of ~1 μA applied through the electrode (Fig. 1h). By measuring the output voltage, the resistance change (ΔR) under illumination was calculated, and the plot in Fig. 1h shows the change in ΔR with respect to the initial resistance (R_o) upon Vis light illumination and the reversal when the light is turned off. The decrease in resistance under illumination may be attributed to the positive temperature coefficient of the electrical conductivity of MnO$_2$ (Fig. S8)[32]. As illumination will induce a temperature rise because of the photothermal property of Co-MnO$_2$ (Fig. S9), the carrier concentration of Co-MnO$_2$ and its conductivity will be increased with the increasing environmental temperature (Fig. S10). The temperature-induced resistance change was verified by directly heating the sensing areas, which revealed a resistance reduction as the temperature increased (Fig. 1h). The magnitude and rate of the resistance change increased when the heater was located closer to the sensing area (Fig. S9). This Au-Ni/Co-MnO$_2$/Au-Ni sensor was used to construct devices with intelligent self-sensing actuation, as will be described in "Microrobotic devices".

Ultrahigh and tunable actuation performance by Co doping

Co-MnO$_2$ actuators exhibit excellent actuation performance in terms of magnitude and actuation and recovery speeds. As an example, for a typical 20-mm long Co-MnO$_2$ actuator prepared from an electrolyte with a Co: Mn ratio of 1:2, a large curvature of 1.75 mm^{-1} corresponding to a cumulative angular deflection of ~2000° at the tip can be induced by near-infrared (NIR) light illumination. As shown in Fig. 2a and Movie S1, a superfast
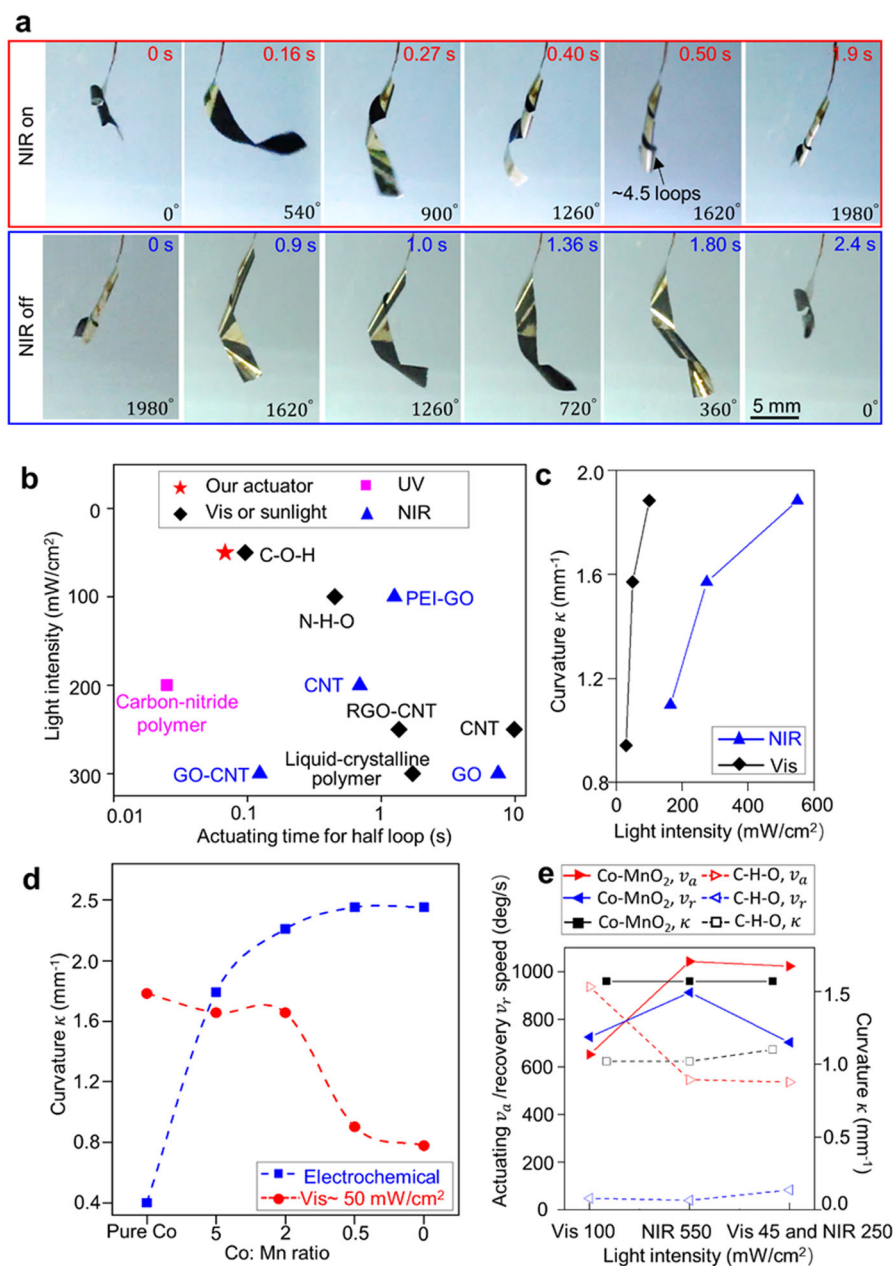
Fig. 2 Actuation performance of Co-MnO₂. **a** Actuation of an actuator with a Co:Mn ratio of 1:2 in the active material induced by an NIR light intensity of 550 mW/cm² at an RH of 95%. **b** Comparison of the performance of a typical actuator (with a Co:Mn ratio of 2:1) in the present work (shown in Movie S1) with that of previously reported light-driven actuators delivering large bending actuation of over 180°; details in Table S1. **c** Actuation performance in response to Vis and NIR light at different light intensities. **d** Influence of the electrolyte ratio of Co:Mn on the electrochemically and light-stimulated actuation performance of Co-MnO₂. **e** Actuation and recovery speeds and curling curvature of Co-MnO₂ (with a Co:Mn ratio of 1:2) and C–O–H actuators under Vis or NIR light.

actuation speed up to 1000°/s with a comparable recovery speed of ~900°/s can be achieved by NIR light with an intensity of 550 mW/cm² under ambient conditions of 24 °C and RH 95%, taking only up to ~100 ms to complete one loop for the first 4.5 loops. Co-MnO₂ can also be effectively triggered by Vis light at a lower intensity. For

the Co-MnO₂ prepared at a Co:Mn ratio of 2:1, a 20-mm long actuator can actuate in response to an ultralow light intensity of ~5 mW/cm² to produce a cumulative angular deflection of 720° at the tip (Fig. S6). At 50 mW/cm², a typical actuator can curl into a loop within ~0.136 s, as shown in Movie S1 and Fig. 2b, exhibiting a maximum

bending angle of ~1080° at the tip for a length of 15 mm. The actuation of Co-MnO$_2$ actuators (with a Co:Mn ratio of 2:1) increases with the light intensity (Fig. 2c), and for the same light intensity, Vis light results in a larger curvature than NIR light.

For electrochemical actuation, Fig. S11 shows the large and fast actuation of a Co-MnO$_2$ actuator in 0.5M Na$_2$SO$_4$ electrolyte when triggered by a potential step (from +1 V for 2 s to actuate to −1 V for 2 s to recover). The speeds for both actuation and recovery were measured to be ~800°/s.

By changing the Co:Mn ratio, the actuation response of Co-MnO$_2$ is found to be modified, as shown in Fig. 2d. Increasing the Co doping amount enhances the light-driven actuation performance, which may be caused by the increased proportion of weakly hydrated water[29]. In contrast, decreasing the Co:Mn ratio enhances the electrochemical actuation and weakens the light-driven response. To demonstrate the complementary actuation in response to electrochemical potential and light stimuli, an open electrodeposition writing method[33] was used to fabricate a prototype film actuator containing two separate muscle groups of different Co:Mn ratios (Fig. S12 and Text S3). The Co-MnO$_2$ layer on the right was prepared from the electrodeposition solution with a lower (1:2) Co:Mn ratio, forming an actuator (H^e) more responsive to electrochemical potential. The left muscle group (H^l) was printed using a higher (5:1) Co:Mn ratio, making it more sensitive to light. Therefore, when an electrochemical potential is applied to both the H^e and H^l actuators, H^e (with lower Co:Mn) exhibits much larger actuation than H^l, while under light stimulation, the performance is reversed (Fig. S12 and Movie S2). Figure 2d shows that upon approaching the pure-Co end of the Co-MnO$_2$ composite system, better light-induced actuation magnitude is achieved. However, as shown in Fig. 2e, the C–O–H system (without Mn) exhibits very sluggish recovery upon light removal even though its light-triggered actuation is fast and large. In contrast, doped Co-MnO$_2$ actuators generally exhibit fast recovery in addition to fast actuation. For example, under Vis light at 100 mW/cm^2, the recovery speed of Co-MnO$_2$ (with a Co:Mn ratio of 1:2) is ~15 times faster than that of C–O–H (Fig. 2e)[34], and under NIR at ~550 mW/cm^2, the recovery speed is ~20 times faster than that of C–O–H.

In Table S4 and Fig. 2b, the actuation time and light intensity requirement of the present Co-MnO$_2$ actuators with Co:Mn = 2:1 are compared with those of other reported light-driven actuators that exhibit a large actuation magnitude of over 180°, and it can be seen that the actuation speed of Co-MnO$_2$ surpasses that of most of the other actuators. Additionally, Co-MnO$_2$ can be effectively powered by common and low-cost Vis light sources of low intensity power, which is an added advantage over other actuators that can only be powered by UV or NIR light of intensity in the hundreds of mW/cm^2. Such a combined merit of superfast, large, and tunable actuation, which is also triggerable by low input power, is utilized in the following to design compact microrobotic systems.
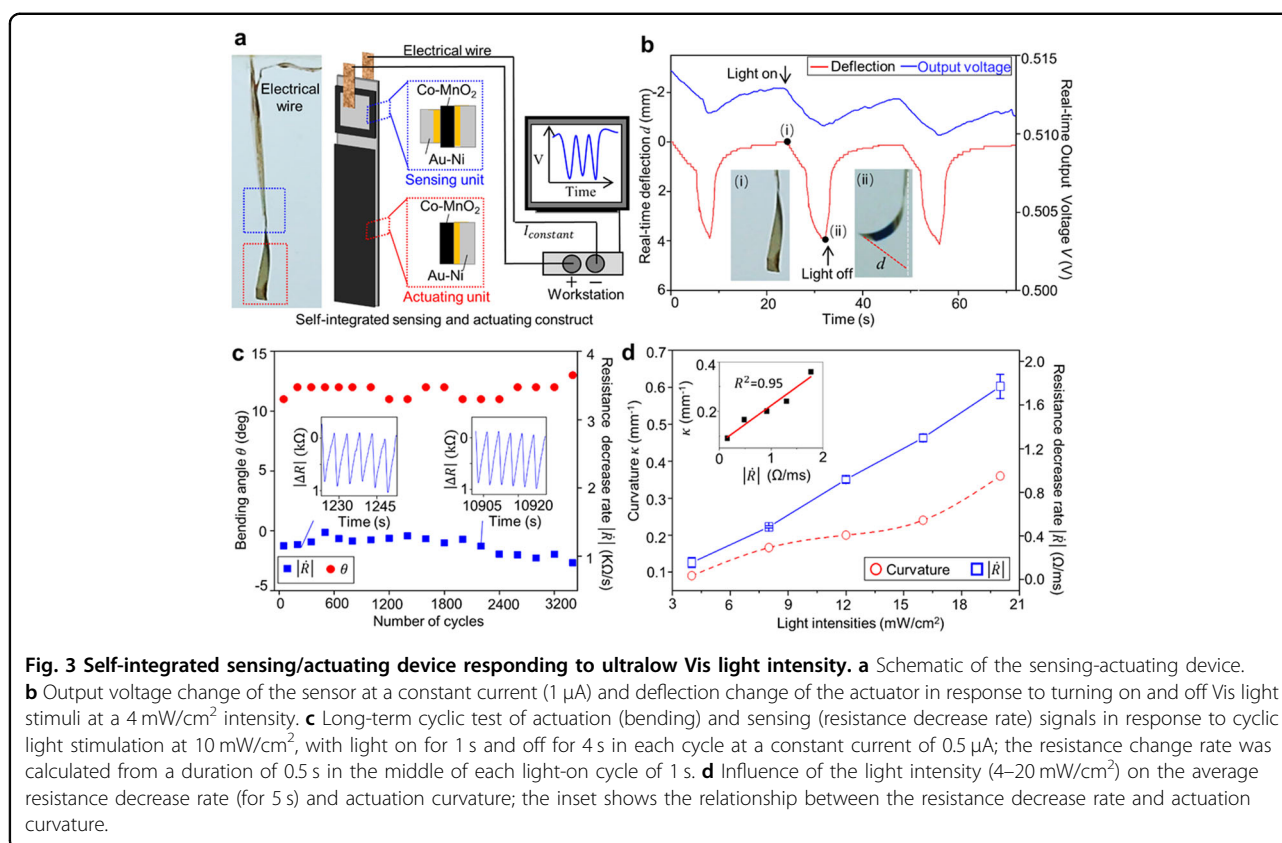
Microrobotic devices
Self-integrated sensing and actuating construct

Here and below, the dual response of actuation and resistance reduction of Co-MnO$_2$ induced by low-power Vis light was utilized to construct smart actuation systems. Figure 3a shows the basic self-integrated sensing and actuating unit fabricated by physically laying a Au-Ni electrode of ~1 cm^2 on top of a Co-MnO$_2$ actuator so that the upper part of the film serves as a light sensor, while the lower part functions as an actuator. Similar to Fig. 1h, a constant current of 1 μA was applied through the multilayer structure, and the voltage output was measured to calculate the resistance. Figure 3b and Movie S3 show a trial run, where light illumination at a 4 mW/cm^2 intensity caused the 15-mm long actuator to bend by ~50° and the voltage to drop by 2.4 mV in a synchronized manner. The corresponding resistance decrease rate ($\dot{R}$) was ~0.16 Ω/ms for the ~1 cm^2 sensing area. The resistance (R) decreased steadily as the light-induced actuation continued, and both the resistance and the deflection signals recovered with removal of the light illumination. To check for consistency of the performance of the unit, long-term cyclic testing was carried out, as shown in Fig. 3c. The resistance and deflection changes were found to be steady over 2000 cycles of light illumination, after which the resistance change rate decreased gradually by ~17%, and for usage as a feedback signal, recalibration would be needed. With increasing light intensity, both the actuation curvature (κ) and $\dot{R}$ increase approximately linearly (Fig. 3d), and κ is approximately proportional to $\dot{R}$, as shown in the inset of Fig. 3d. The easy read-out of $\dot{R}$ and its linear relationship with the light intensity render it a very useful feedback signal for the design of a circuit to control the actuation performance, as shown in the following sections.

Smart load-lifting system

The design of the self-integrated sensing-actuating unit in Fig. 3 was utilized, as shown in Fig. 4a, to construct an intelligent load-lifting robot with a lifting capability unaffected by environmental disturbances. Here, on a supporting layer 8 mm × 32 mm large, the top part was electrodeposited with Co-MnO$_2$ to form a sensing unit by further laying a Au-Ni electrode on it. The sensor area was 5 mm × 5 mm, and the actuating unit consisted of a pair of Co-MnO$_2$ hinges of 8 mm × 4 mm electrodeposited as shown, which could lift an object vertically

Fig. 3 Self-integrated sensing/actuating device responding to ultralow Vis light intensity. a Schematic of the sensing-actuating device. **b** Output voltage change of the sensor at a constant current (1 µA) and deflection change of the actuator in response to turning on and off Vis light stimuli at a 4 mW/cm² intensity. **c** Long-term cyclic test of actuation (bending) and sensing (resistance decrease rate) signals in response to cyclic light stimulation at 10 mW/cm², with light on for 1 s and off for 4 s in each cycle at a constant current of 0.5 µA; the resistance change rate was calculated from a duration of 0.5 s in the middle of each light-on cycle of 1 s. **d** Influence of the light intensity (4–20 mW/cm²) on the average resistance decrease rate (for 5 s) and actuation curvature; the inset shows the relationship between the resistance decrease rate and actuation curvature.
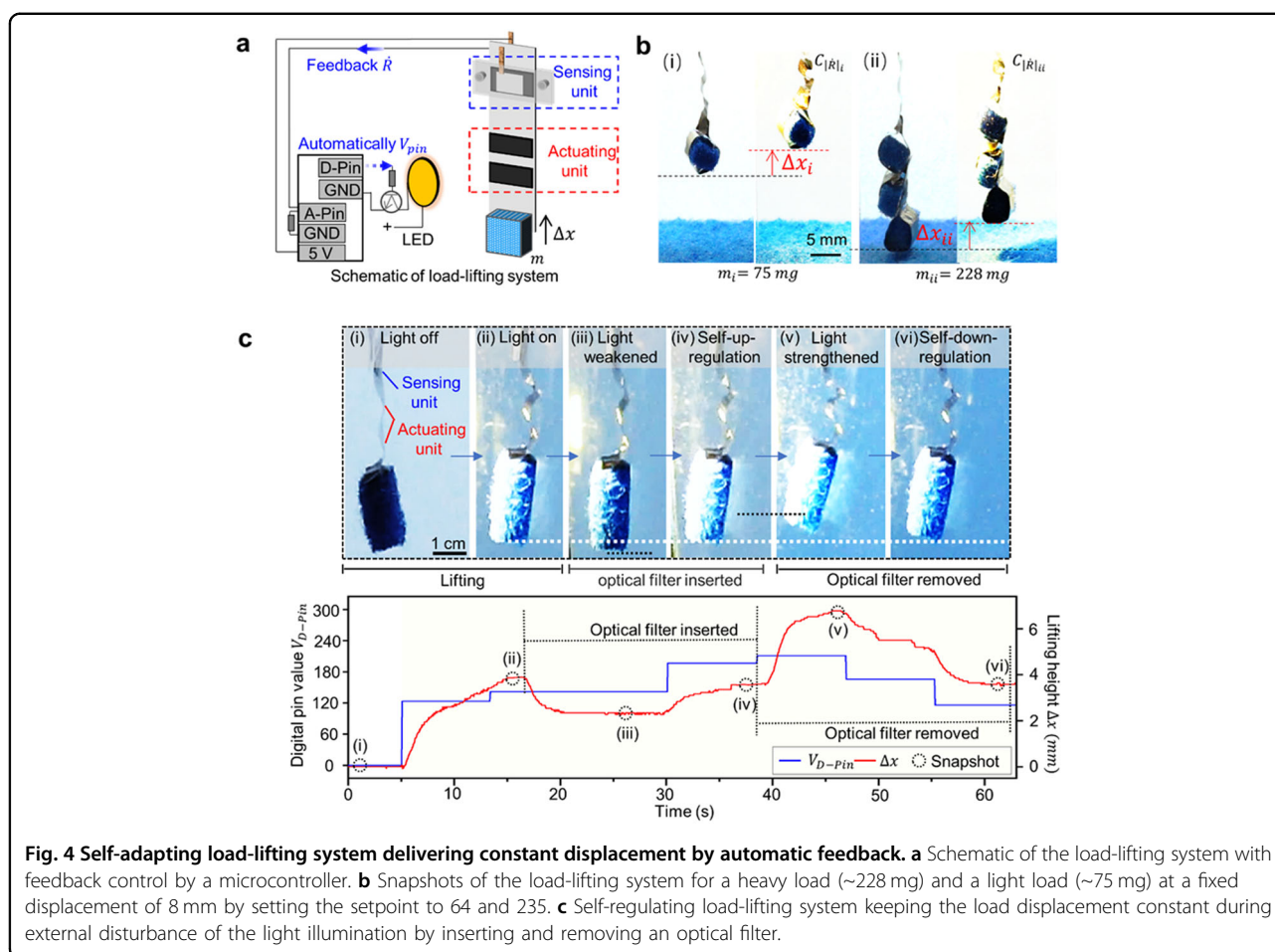
when triggered by light illumination. Here, the same LED light source illuminated both the sensor and the actuator, and the resistance decrease rate $\dot{R}$ from the sensor was used as a feedback signal to control the light intensity via a microcontroller so that the correct light intensity was always incident on the actuator to make it lift a certain load to a given height. Because of the linear relationship between the light intensity and $\dot{R}$ (Fig. 3d), a basic proportional control for the light source was used, with a proportional gain parameter K_P ~0.8 between the light intensity and $\dot{R}$ as deduced from Fig. S13 (see Supporting Text S4 in the Supplementary information for further details about the control).

By determining the light intensity needed to lift different loads to different heights, the setpoints $C_{|\dot{R}|}$ for feedback control of the light source were precalibrated. Figure 4b shows that with feedback control of the light source, the device could raise two different loads to approximately the same height Δx. The first load (m_i) had a weight of ~75 mg, and the Co-MnO$_2$ actuating material in the device had a weight of ~0.44 mg, given that its volume is ~ $2 \times 0.4 \times 0.8 \times 0.0002$ cm^3 and the density of birnessite-type MnO$_2$ is ~3.4 g/cm^3. Because of the high actuation performance of Co-MnO$_2$, the heavy load was lifted by ~8 mm in response to the relatively low Vis light

illumination of ~13 mW/cm² provided by the preset value of $C_{|\dot{R}|_i}$, as shown in Fig. 4b. Utilizing the roughly linear relationship among the lifting capability, the light intensity and the real-time $|\dot{R}|$, for a load (m_{ii}) of ~228 mg (~3 times m_i), $C_{|\dot{R}|_{ii}}$ was then preset at roughly three times $C_{|\dot{R}|_i}$ to accomplish the same Δx of ~8 mm (Fig. 4b and Movie S4).

The intelligence of the load-lifting system lies in its ability to maintain a given load at the same height when the light illumination is externally disturbed (Fig. 4c and Movie S5). In the demonstration in Fig. 4c, between snapshots (i) and (ii), the system searched for the correct light intensity (from the initial "off" state at (i)) to raise a load of ~50 mg to a height Δx of ~4 mm; this was achieved upon approaching point (ii) when the digital pin value V_{D-pin} (blue line in Fig. 4c) of the microcontroller that set the power input to the LED source reached the value corresponding to the setpoint $C_{|\dot{R}|}$ of the $|\dot{R}|$ signal from the sensor. Then, at point (ii), a light filter (with attenuation rate ~50%) was inserted between the light source and the sensing-lifting device to weaken the actual light intensity incident on the latter. Such a disturbance decreased Δx and the real-time feedback $|\dot{R}|$ (point (iii)). Due to the decreased $|\dot{R}|$ signal, the microcontroller then
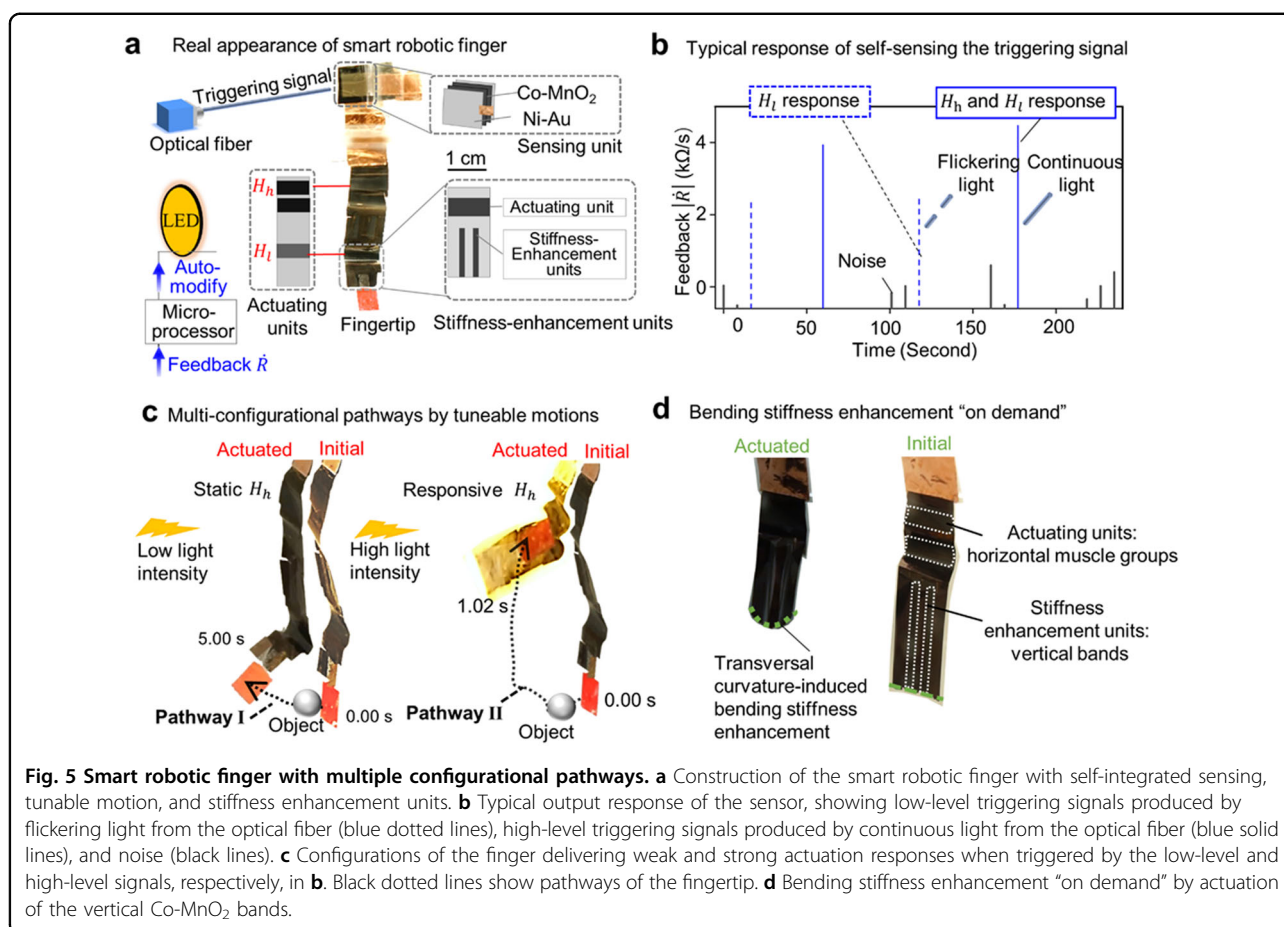
Fig. 4 Self-adapting load-lifting system delivering constant displacement by automatic feedback. a Schematic of the load-lifting system with feedback control by a microcontroller. **b** Snapshots of the load-lifting system for a heavy load (~228 mg) and a light load (~75 mg) at a fixed displacement of 8 mm by setting the setpoint to 64 and 235. **c** Self-regulating load-lifting system keeping the load displacement constant during external disturbance of the light illumination by inserting and removing an optical filter.

upregulated the V_{D-pin} signal until Δx and $|\dot{R}|$ regained the preset values (point (iv) in Fig. 4c). After a steady state was reached, the optical filter was removed to mimic another disturbance. The light intensity illuminating the lifting system then strengthened, as did Δx and $|\dot{R}|$ (point (v)). The microcontroller then automatically decreased the light intensity until Δx and $|\dot{R}|$ dropped back to the preset values (point (vi)). This demonstrates the self-adapting capability of the smart load-lifting system with integrated sensor and actuator made of the same Co-MnO$_2$ material in response to environmental disturbances.

Smart robotic finger with feedback-controlled multiple configurational pathways

Next, we demonstrate a microrobotic finger that can perform motions of different degrees of freedom via multiple configurational pathways, selected by different triggering signals sent to the sensor by the same optical fiber. "Ultrahigh and tunable actuation performance by Co doping" section and Fig. S12 show that by integrating Co-MnO$_2$ muscle groups of different Co:Mn ratios into the same construct, different motions can be achieved.

Utilizing this concept, a robotic finger, as shown in Fig. 5a, was built, with a sensing unit on the top and two sets of horizontal hinges of Co-MnO$_2$ as the actuating units. The sensor receives a triggering light signal delivered by an optical fiber, and the corresponding resistance change $\dot{R}$ is fed into the microcontroller, which outputs a current to power a separate LED light source that provides illumination to the Co-MnO$_2$ muscle groups to actuate them. The two muscle groups were made of materials with different Co:Mn ratios and therefore would actuate to different extents to configure the finger along different configurational pathways. The upper actuating hinge, denoted as H_h, had a lower Co:Mn ratio of 1:2 that could only be efficiently stimulated by a high light intensity from the LED source, and the other, denoted as H_l, was prepared with a higher Co:Mn ratio of 5:1 so that it could be actuated by low light intensity. As the finger was extremely compact (<5 μm) and therefore compliant, two vertical bands of Co-MnO$_2$ were electrodeposited to enhance the stiffness, as detailed below. To operate the system, the optical fiber sends a triggering light signal to the sensor, and the resultant resistance change signal $\dot{R}$ is

Fig. 5 Smart robotic finger with multiple configurational pathways. a Construction of the smart robotic finger with self-integrated sensing, tunable motion, and stiffness enhancement units. **b** Typical output response of the sensor, showing low-level triggering signals produced by flickering light from the optical fiber (blue dotted lines), high-level triggering signals produced by continuous light from the optical fiber (blue solid lines), and noise (black lines). **c** Configurations of the finger delivering weak and strong actuation responses when triggered by the low-level and high-level signals, respectively, in **b**. Black dotted lines show pathways of the fingertip. **d** Bending stiffness enhancement "on demand" by actuation of the vertical Co-MnO$_2$ bands.

fed back to the microcontroller and is classified into one of three categories: (1) noise, (2) low-level, or (3) high-level signals. Any noise signal is ignored and not used to regulate the LED light source. A signal classified as low level is used to provide a low current output to the LED light source to actuate the H_l muscle group, and similarly, a received high-level signal is used to provide a high current to the LED source to actuate both the H_l and H_h muscle groups to deliver fast and large motions within ~1 s. Figure 5b shows a typical response of the sensor in action; here, the sensor was stimulated by optical fiber light signals of two types: a low-level type of discrete (flickering) illumination and a high-level type of continuous illumination. The two types of signals were delivered manually and sporadically by switching on and off the optical fiber, and the corresponding $\dot{R}$ responses are shown in Fig. 5b, where dotted blue lines represent the low-level signals and solid blue lines the high-level signals. Random, ultralow signals (black lines) that did not correspond to the manually delivered optical fiber signals were also recorded by the sensor, and these were regarded as noise. Figure 5c and Movie S6 show the corresponding

movements of the finger, where the black dotted lines in Fig. 5c indicate the trajectories of the fingertip under the low- and high-level stimuli. The two modes of motion allow the same fingertip to touch objects placed at very different positions in space, as illustrated in Fig. 5c. The stability of the smart finger was investigated by cyclic stimulations (see Text S5 for details), and the results, shown in Figure S14, indicate high stability in the performance over 150 cycles of repeated stimulation.

As mentioned above, in addition to the horizontal muscle groups H_l and H_h, additional vertical bands of Co-MnO$_2$ were also coated onto the substrate to enhance the structural stiffness in an active, on-demand manner. When illuminated by LED light, the vertical bands would also actuate, thus bending the passive layer about the vertical axis (Fig. 5d) to increase the bending stiffness of the finger as a load-bearing cantilever structure (see Text S6 and Fig. S15 for details). It is of interest to note that the stiffening achieved in this way is "on-demand", i.e., the stiffening is provided by the actuation of the vertical Co-MnO$_2$ bands only when the finger is triggered by light to lift a load.
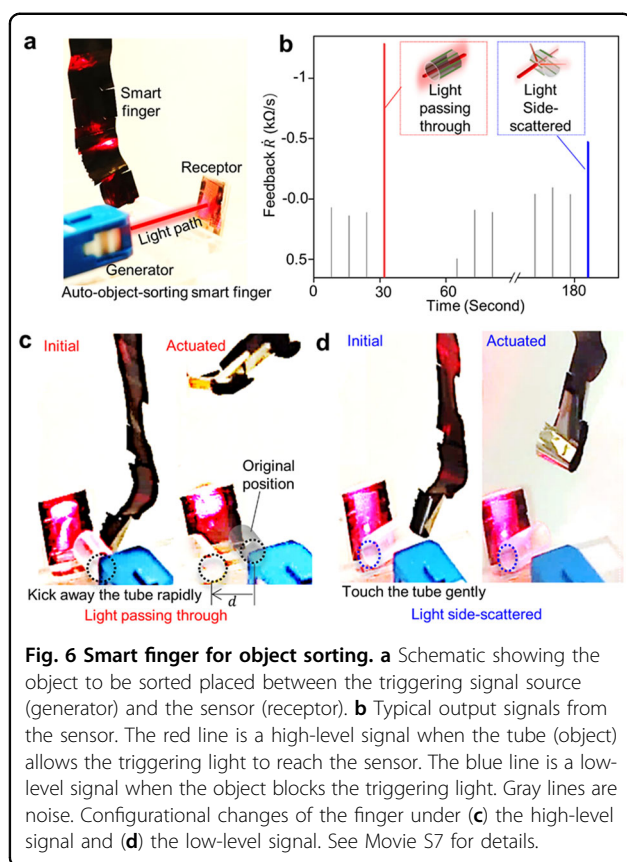
Fig. 6 Smart finger for object sorting. a Schematic showing the object to be sorted placed between the triggering signal source (generator) and the sensor (receptor). **b** Typical output signals from the sensor. The red line is a high-level signal when the tube (object) allows the triggering light to reach the sensor. The blue line is a low-level signal when the object blocks the triggering light. Gray lines are noise. Configurational changes of the finger under (**c**) the high-level signal and (**d**) the low-level signal. See Movie S7 for details.

Figure 6 shows a modified design of the smart finger for performing the object-sorting function. As shown in Fig. 6a, the sensor was placed at the bottom of the finger, and as before, horizontal $Co-MnO_2$ muscle groups and vertical $Co-MnO_2$ strengtheners were coated to actuate the finger. The object to be sorted had the form of a small transparent tube marked with colored strips, and it was placed between the triggering signal-delivering optical fiber (generator) and the sensor (receptor). When the tube axis aligns with the optical fiber, the light signal will pass through the tube and illuminate the sensor, thus producing a "high-level" signal, as shown by the red line in Fig. 6b. Both the H_h and H_l muscle groups will be actuated by the microcontroller, and the finger will rapidly kick away the tube (by distance d, as shown in Fig. 6c; see Movie S7 for details). On the other hand, if the tube axis does not align well with the light delivered by the optical fiber, as shown in Fig. 6b, then the light is side-scattered by the tube, and hence, the sensor will record a "low-level" signal, as shown by the blue line in Fig. 6d. In this case, the microcontroller will send a low current to the LED source to actuate only the H_l muscle group, causing the finger to only gently touch the tube.

The smart fingers in Figs. 5 and 6 demonstrate the versatility of the tunable actuation of $Co-MnO_2$ and its

high sensitivity to small differences in Vis light intensity (down to ~5 mW/cm^2 differences, as in Fig. 3d) in designing intelligent and compact devices.

Discussion

In this work, the concept of using a multistimuli-responsive material to create robotic intelligence to achieve unprecedented functionalities is established using $Co-MnO_2$ as a high-performing, high-versatility actuating material. The merits of $Co-MnO_2$ are summarized as follows.

High actuation performance

As shown in Fig. 2b, the ultrafast actuation (~100 ms for one loop) with low required power (~0.5 sun) makes it a good actuating material for microrobotics applications. In particular, the light-induced actuation is activated by a novel electrochemical treatment that increases the affinity of $Co-MnO_2$ to water molecules via the incorporation of Na^+. Doping with Co further increases the light-induced actuation performance (Fig. 2d), which also overcomes the slow recovery problem of previously developed dual-responsive actuators[5,34–36]. The energy conversion efficiency of the actuator and the force generated by the actuator under a visible light intensity of 100 mW/cm^2 are estimated to be ~0.1% and ~23 μN, respectively (see Text S7).

High versatility

In addition to actuation induced by light, a light-induced resistivity change property of $Co-MnO_2$ is also discovered and found to be versatile in feedback control of the actuation. The sensing properties are more applicable to the low light intensity regime (Fig. S16), and since the sensing and actuating units are independent, a rather large light spot is needed to trigger both units. This problem can be alleviated in future work by electro-depositing $Co-MnO_2$ on a conductive layer with a strain-sensing function so that the actuating and sensing units can be combined in a much more compact manner. In the devices in Figs. 4–6, a microcontroller is still needed (just as in animals where a brain is still needed to control voluntary muscles), but the dual response of $Co-MnO_2$ in terms of both actuation and resistance change allows essentially the same compact thin-film construct to function as both an artificial muscle and a sensor, and this already greatly reduces the complexity and bulkiness of the device. Furthermore, the tunable actuation performance in Fig. 2d presents another major advantage of the $Co-MnO_2$ material system, which can be exploited to allow muscles of different capabilities to be integrated into the same compact construct, as in the case of a small animal. The one-stimulus, multiresponsive nature found in $Co-MnO_2$ here is seldom studied and has never been

utilized in robotics applications in the past, although some other materials are known to exhibit the reverse behavior of a single response to multiple stimuli, such as carbon nanotubes[37,38].

In summary, the dual response of actuation and resistance reduction induced by visible light in Co-MnO$_2$ is utilized to realize intelligent functions, including self-adapting lifting, multiple pathway motion, and on-demand stiffness control. Activated by a novel electrochemical treatment, the light actuation of Co-MnO$_2$ exhibits high performance in terms of actuation magnitude (curvatures up to 1.7 mm^{-1}) and speed (~100 ms for 1 loop) in response to low-intensity Vis light stimuli, with symmetrical actuation and recovery speeds. The actuation response is tunable by controlling the Co:Mn ratio, and easy fabrication by masked or open electrodeposition allows the construction of a myriad of intelligent robotic devices. The devices presented in this paper are only some examples of the myriad of new functionalities that can be designed. For instance, only the light-triggered responses of Co-MnO$_2$ are utilized in the present work, and in the future, the responses induced by electrochemical potentials, heat, and humidity changes can also be studied.

Author contributions
A.H.W.N. supervised the overall research. K.W.K. and R.W. conceptualized the Co-MnO$_2$ actuating-sensing system and investigated the doping effect. K.W.K., R.W. and C.H.M. developed the Co-MnO$_2$ actuating-sensing system. R.W. performed experiments and collected the data. R.W., K.W.K. and A.H.W.N. performed the analysis and wrote the paper.

Conflict of interest
The authors declare no competing interests.

References
1. McCracken, J. M., Donovan, B. R. & White, T. J. Materials as machines. *Adv. Mater.* **32**, 1906564 (2020).
2. Hines, L., Petersen, K., Lum, G. Z. & Sitti, M. Soft actuators for small-scale robotics. *Adv. Mater.* **29**, 1603483 (2017).
3. Wang, J., Li, S., Gao, D., Xiong, J. & Lee, P. S. Reconfigurable and programmable origami dielectric elastomer actuators with 3D shape morphing and emissive architectures. *NPG Asia Mater.* **11**, 1–7 (2019).
4. Hu, Y. et al. Electrically and sunlight-driven actuator with versatile biomimetic motions based on rolled carbon nanotube bilayer composite. *Adv. Funct. Mater.* **27**, 1704388 (2017).
5. Kwan, K. W. et al. Light-stimulated actuators based on nickel hydroxide-oxyhydroxide. *Sci. Robot.* **3**, eaat4051 (2018).
6. Lim, H. et al. Construction of a photothermal Venus flytrap from conductive polymer bimorphs. *NPG Asia Mater.* **9**, e399 (2017).
7. Yang, Y., Liu, Y. & Shen, Y. Plasmonic-assisted graphene oxide films with enhanced photothermal actuation for soft robots. *Adv. Funct. Mater.* **30**, 1910172 (2020).
8. Han, B. et al. Plasmonic-assisted graphene oxide artificial muscles. *Adv. Mater.* **31**, 1806386 (2019).
9. Amjadi, M. & Sitti, M. High-performance multiresponsive paper actuators. *ACS Nano* **10**, 10202–10210 (2016).
10. Kim, Y., Yuk, H., Zhao, R., Chester, S. A. & Zhao, X. Printing ferromagnetic domains for untethered fast-transforming soft materials. *Nature* **558**, 274–279 (2018).
11. Cai, G., Ciou, J. H., Liu, Y., Jiang, Y. & Lee, P. S. Leaf-inspired multiresponsive MXene-based actuator for programmable smart devices. *Sci. Adv.* **5**, eaaw7956 (2019).
12. Weng, M. et al. Electric-fish-inspired actuator with integrated energy-storage function. *Nano Energy* **68**, 104365 (2020).
13. Zhou, P. et al. Monolithic superaligned carbon nanotube composite with integrated rewriting, actuating and sensing multifunctions. *Nano Res.* **12**, 1–7 (2021).
14. Amjadi, M., Turan, M., Clementson, C. P. & Sitti, M. Parallel microcracks-based ultrasensitive and highly stretchable strain sensors. *ACS Appl. Mater. Interfaces* **8**, 5618–5626 (2016).
15. Wang, X. Q. et al. Somatosensory, light-driven, thin-film robots capable of integrated perception and motility. *Adv. Mater.* **32**, 2000351 (2020).
16. Truby, R. L. et al. Soft somatosensory actuators via embedded 3D printing. *Adv. Mater.* **30**, 1706383 (2018).
17. Phan, H. P. et al. Self-sensing paper-based actuators employing ferromagnetic nanoparticles and graphite. *Appl. Phys. Lett.* **110**, 144101 (2017).
18. Larson, C. et al. Highly stretchable electroluminescent skin for optical signaling and tactile sensing. *Science* **351**, 1071–1074 (2016).
19. Lu, H., Hong, Y., Yang, Y., Yang, Z. & Shen, Y. Battery-less soft millirobot that can move, sense, and communicate remotely by coupling the magnetic and piezoelectric effects. *Adv. Sci.* **7**, 2000069 (2020).
20. Zhao, H., O'Brien, K., Li, S. & Shepherd, R. F. Optoelectronically innervated soft prosthetic hand via stretchable optical waveguides. *Sci. Robot.* **1**, eaai7529 (2016).
21. Zhao, P., Xu, B., Zhang, Y., Li, B. & Chen, H. Study on the twisted and coiled polymer actuator with strain self-sensing ability. *ACS Appl. Mater. Interfaces* **12**, 15716–15725 (2020).
22. Wang, C. et al. Soft ultrathin electronics innervated adaptive fully soft robots. *Adv. Mater.* **30**, 1706695 (2018).
23. Yang, H. et al. Multifunctional metallic backbones for origami robotics with strain sensing and wireless communication capabilities. *Sci. Robot.* **4**, eaax7020 (2019).
24. Cheng, H. et al. One single graphene oxide film for responsive actuation. *ACS Nano* **10**, 9529–9535 (2016).
25. Chen, L. et al. Graphene-based actuator with integrated-sensing function. *Adv. Funct. Mater.* **29**, 1806057 (2019).
26. Amjadi, M. & Metin, S. Self-sensing paper actuators based on graphite–carbon nanotube hybrid films. *Adv. Sci.* **5**, 1800239 (2018).
27. Gorlin, Y. et al. In situ X-ray absorption spectroscopy investigation of a bifunctional manganese oxide catalyst with high activity for electrochemical water oxidation and oxygen reduction. *J. Am. Chem. Soc.* **135**, 8525–8534 (2013).
28. Liu, L. et al. The origin of electrochemical actuation of MnO$_2$/Ni bilayer film derived by redox pseudocapacitive process. *Adv. Funct. Mater.* **29**, 1806776 (2019).
29. Matsui, H., Ju, J., Odaira, T. & Toyota, N. Two-dimensionally confined water in between MnO$_2$ layers of Na-birnessite. *J. Phys. Soc. Jpn.* **78**, 074801–074801 (2009).
30. Shan, X. et al. Structural water and disordered structure promote aqueous sodium-ion energy storage in sodium-birnessite. *Nat. Commun.* **10**, 4975 (2019).

31. Cai, J., Liu, J. & Suib, S. L. Preparative parameters and framework dopant effects in the synthesis of layer-structure birnessite by air oxidation. *Chem. Mater.* **14**, 2071–2077 (2002).

32. Bhide, V. G. & Dan, R. H. Electrical conductivity in oxides of manganese and related compounds. *Physica* **27**, 821–826 (1961).

33. Wu, R., Kwan, K. W., Ma, W., Wang, P. & Ngan, A. H. W. Self-actuating origamis realized by independently printable and controllable stimuli-responsive creases. *Appl. Mater. Today* **20**, 100621 (2020).

34. Kwan, K. W. & Ngan, A. H. W. A high-performing, visible-light-driven actuating material responsive to ultralow light intensities. *Adv. Mater. Technol.* **4**, 1900746 (2019).

35. Kwan, K. W. & Ngan, A. H. W. Visible-light-driven, nickel-doped cobalt oxides/hydroxides actuators with high stability. *ACS Appl. Mater. Interfaces* **12**, 30557–30564 (2020).

36. Kwan, K. W., Hau, N. Y., Feng, S. P. & Ngan, A. H. W. Electrochemical actuation of nickel hydroxide/oxyhydroxide at sub-volt voltages. *Sens. Actuators B Chem.* **248**, 657–664 (2017).

37. Lima, M. D. et al. Electrically, chemically, and photonically powered torsional and tensile actuation of hybrid carbon nanotube yarn muscles. *Science* **338**, 928–932 (2012).

38. Li, J. et al. Multi-responsive and multi-motion bimorph actuator based on super-aligned carbon nanotube sheets. *Carbon* **148**, 487–495 (2019).